

CFD Calculation of Stability and Control Derivatives For Ram-Air Parachutes

Mehdi Ghoreyshi^{1*}, Keith Bergeron^{2†}
Andrew J. Lofthouse^{1‡}; Russell M. Cummings^{1§}

¹ *High Performance Computing Research Center, U.S. Air Force Academy
USAF Academy, Colorado 80840*

² *US Army Natick Research, Development, and Engineering Center
Natick, MA 01760*

Generation of aerodynamic models for ram-air parachutes is currently the subject of active research. These parachutes resemble a rectangular wing of low aspect ratio. The aerodynamic characteristics of these unswept wings can be very different from those predicted by lifting-line theory due to openings in the leading edge for the admission of ram air. This research specifically investigates the aerodynamics of ram-air parachutes with open and closed round inlets. All wings are assumed to be rigid and have an aspect ratio of two. Aerodynamic predictions are made with flow solvers of Cobalt and Kestrel and are compared with available wind-tunnel experimental data. Simulations and measurements are carried out at a Mach number of 0.25 and Reynolds number of 1.4 million. The aerodynamic changes are predicted due to pulling the left trailing edge down. Aerodynamic stability derivatives are calculated from simulations of forced periodic motions in directions of pitch, yaw, and roll. The effects of motion reduced frequency are studied as well. Two different estimation methods are used, namely linear regression method and a method based on points of maximum and minimum angular velocity. The experimental data of wings considered here match the computational predictions quite well. For the wings with a left-side bending, the lift and drag will increase, the pitch moment at the quarter chord point will decrease and wing will produce a positive roll and a negative yaw moment. The open wings stall earlier than the closed wings, have higher pressure-drag values, and the pitch moment slope becomes more negative. The calculated derivatives are similar for both methods and show only a small change with reduced frequencies less than 0.1. The results show that damping derivatives of closed wings remain fairly constant up to ten degrees angle of attack. However, the open wings show a very sensitive behavior in damping derivatives with respect to angles of attack. Finally, the models are evaluated for the closed and open wings undergoing a chirp motion. The results of the comparison show that the aerodynamic models of the closed wing match time-marching full CFD calculations well, but some discrepancies can be seen in the open wing plots. The lift values from model and full CFD do not match everywhere and there is a time lag between pitch moment predictions and time-marching solution, suggesting substantial unsteady effects on the numerical simulations of open wings during the motion.

*Senior Aerospace Engineer, AIAA Senior Member

†Senior Research Aerospace Engineer, AIAA Senior Member

‡Director, AIAA Senior Member

§Professor of Aeronautics, AIAA Associate Fellow

“The views expressed in this paper are those of the author and do not reflect the official policy or position of the United States Air Force, Department of Defense, or the U.S. Government.” Distribution A. Approved for Public Release. Distribution unlimited.

Nomenclature

A	motion amplitude, rad
a	speed of sound, m/s
b	wing span, m
C_D	drag coefficient, $D/q_\infty S$
C_L	lift coefficient, $L/q_\infty S$
$C_{L\alpha}$	lift coefficient curve slope, 1/rad
C_{M_x}	roll moment coefficient, $M_x/q_\infty S b$
$C_{M_x\beta}$	derivative of roll moment coefficient with respect to sideslip angle, 1/rad
C_{M_y}, C_m	pitch moment coefficient, $M_y/q_\infty S c$
$C_{M_y\alpha}$	pitch moment coefficient curve slope, 1/rad
C_{M_z}	yaw moment coefficient, $M_z/q_\infty S b$
$C_{M_z\beta}$	derivative of yaw moment coefficient with respect to sideslip angle, 1/rad
C_p	pressure coefficient
C_Y	side-force coefficient, $Y/q_\infty S$
$C_{Y\beta}$	derivative of side-force coefficient with respect to sideslip angle, 1/rad
c	mean aerodynamic chord, m
D	drag force, N
f	frequency, Hz
k	reduced frequency, $\omega c/2V$
L	lift force, N
M_x	roll moment, N-m
M_y	pitch moment, N-m
M_z	yaw moment, N-m
M	Mach number, V/a
PDF	pitch damping force, 1/rad, $C_{Lq} + C_{L\dot{\alpha}}$
PDM	pitch damping moment, 1/rad, $C_{M_yq} + C_{M_y\dot{\alpha}}$
$\bar{p}, \bar{q}, \bar{r}$	roll, pitch, and yaw rates, rad/s
p	normalized roll rate, $\bar{p}b/2V$
q	normalized pitch rate, $\bar{q}c/2V$
RDF	roll damping force, 1/rad, C_{Yp}
RDM1	roll damping of roll moment, 1/rad, C_{M_xp}
RDM2	roll damping of yaw moment, 1/rad, C_{M_zp}
r	normalized yaw rate, $\bar{r}b/2V$
q_∞	dynamic pressure, Pa, $\rho V^2/2$
Re	Reynolds number, $\rho V c/\mu$
S	Planform area, m ²
V	freestream velocity, m/s
x, y, z	aircraft position coordinates
YDF	yaw damping force, 1/rad, $C_{Yr} + C_{Y\dot{\beta}}$
YDM1	yaw damping of roll moment, 1/rad, $C_{M_xr} + C_{M_x\dot{\beta}}$
YDM2	yaw damping of yaw moment, 1/rad, $C_{M_zr} + C_{M_z\dot{\beta}}$

Greek

α	angle of attack, rad
$\dot{\alpha}$	time-rate of change of angle of attack, rad/s
β	sideslip angle, rad
$\dot{\beta}$	time-rate of change of side-slip angle, rad/s
δ	trailing edge deflection angle, rad
ϕ	roll (bank) angle, rad
ρ	air density, kg/m ³
μ	air viscosity, kg/(m.s)
ω	angular velocity, rad/s

I. Introduction

The U.S. Army Natick Soldier Center manages and coordinates the DoD program to develop precision guided airdrop systems known as the Joint Precision Airdrop System (JPADS). JPADS provides the ability to deliver to multiple drop zones as quickly as possible, reduces the ground resupply risks and costs, and also allows the delivery aircraft to avoid hazardous objective areas.¹ JPADS has shown very promising results, but there is still an increasing demand for enhancing the reliability and landing precision of these airdrop systems. This is a very challenging task because these systems are expected to operate from altitudes up to 35,000 feet and to have a release point up to 40 km from the drop zone.^{2,3}

Current precision aerial delivery systems use a large ram-air parachute (parafoil) integrated with a Global Positioning System (GPS) equipment, a navigation and a control system.⁴ These airdrop designs could achieve a landing accuracy of 100 meters or even less depending on the control unit performance.⁴ The control performance will also depend on the accuracy of aerodynamic models for various drop conditions.

The aerodynamic models used in the design of parafoils are typically empirical or semi-empirical methods generated from wind tunnel experiments and drop tests.⁵ For novel parachute designs, there are no experimental data available to design control laws. Parachute designers might use the low-speed wing aerodynamic to estimate the lift and drag coefficients.^{6,7} However, these estimates can yield very different results from those measured in tests due to openings in the leading edge of parachutes for the admission of ram air. As noted in the previous studies,^{8,9,10,11} for a given shape, the open wings have different aerodynamic characteristic than the closed wings.

There is a new focus on generation of aerodynamic models of ram-air parachutes using Computational Fluid Dynamics(CFD) simulations. This study is a continuation of previous collaborations between U.S. Air Force Academy (USAFA) and the U.S. Army Natick Soldier Center (NSC) on the application of CFD for design and simulation of new ram-air parachutes. A previous publication by the authors has attempted to generate CFD-based aerodynamic models for flight simulation of ram-air parachutes.¹¹ The parachute geometries were modeled as rigid rectangular wings with an aspect ratio of two and zero anhedral angle. A linear regression model was used to estimate the stability derivatives from forced periodic motions. These derivatives were only estimated at eight degrees angle of attack. The results showed that the models match full CFD data which were used to create the models.

This study extends these previous results by calculation of stability derivative at different angles of attack and investigating the effects of motion frequency on stability derivatives. CFD predictions are validated with additional experimental data. Two different estimation methods are used in this work, namely linear regression method and a method based on points of maximum and minimum angular velocity. Longitudinal predictions are found from pitching and plunging motions using Cobalt and Kestrel flow solvers. Finally, the models are tested for a chirp motion that is not used to create the aerodynamic models. The chirp's amplitude is constant but its frequency increases with time. This specific motion can exhibit time and frequency dependent behavior and lag effects for these wing configurations.

The wings are again assumed to be rigid and have an aspect ratio of two. Aerodynamic predictions are made with flow solvers of Cobalt and Kestrel and are compared with available wind-tunnel experimental data. Simulations and measurements are carried out at a Mach number of 0.25 and Reynolds number of 1.4 million. The effects of pulling the left trailing edge down on the aerodynamic data are also investigated. The aerodynamic models are assumed to be a linear function of input parameters. The model coefficients, the so-called aerodynamic derivatives, are found by two identification methods from CFD simulations of forced oscillation motions. The changes in derivatives with changes in angle of attack and reduced frequency are studied. Notice that a frequency-dependent behavior cannot be reconciled with the stability derivatives model.¹² A chirp motion is used to assess models. This is a large amplitude with varying frequency motion and therefore can highlight the limitations of the models.

This work is organized as follows: first the flow solvers and system identification methods are reviewed. Test cases, the computational grids, and experimental setup are presented next. The results are then presented and discussed, followed by the concluding remarks.

II. Calculation of Stability Derivatives

In this work, the stability derivatives are calculated by imposing a forced sinusoidal motion around the wing's quarter point. A pitching sinusoidal motion is defined as:

$$\alpha = \alpha_0 + A \sin(\omega t) \quad (1)$$

where α_0 and A are the mean angle and amplitude, respectively; $\omega = 2\pi f$ is angular velocity. The time rate change of angle of attack is the pitch rate and is written as:

$$\bar{q} = \dot{\alpha} = \omega A \cos(\omega t) \quad (2)$$

the normalized pitch rate is then defined as:

$$q = \frac{\bar{q}c}{2V} \quad (3)$$

These motions can likewise be written in directions of yaw and roll. For calculation of stability derivatives, it is assumed that the aerodynamic coefficients are linear functions of inputs. The aerodynamic forces and moments for a body fixed axes are shown in Figure 1. Let's denote $C_L, C_D, C_Y, C_{Mx}, C_{My}, C_{Mz}$ as lift, drag, side force, roll, pitch, and yaw moment coefficients, respectively. Angles of attack and sideslip are shown with α and β . Therefore, $\dot{\alpha}, \dot{\beta}$ denote the time-rate of change of angle of attack and side slip angle. Normalized roll, pitch, and yaw rates are shown with p, q, r . During a forced-oscillation pitch, the lift and pitch moment can be written as:

$$\begin{aligned} C_L &= C_{L0} + C_{L\alpha}(\alpha - \alpha_0) + (C_{L\dot{\alpha}} + C_{Lq})q \\ C_{My} &= C_{My0} + C_{My\alpha}(\alpha - \alpha_0) + (C_{My\dot{\alpha}} + C_{Myq})q \end{aligned} \quad (4)$$

where terms with zero subscript represent the values at the mean angle of attack. For a forced-oscillation in yaw direction starting at zero sideslip angle, the lateral coefficients are formulated as:

$$\begin{aligned} C_Y &= C_{Y0} + C_{Y\beta}\beta + (C_{Yr} - C_{Y\dot{\beta}})r \\ C_{Mx} &= C_{Mx0} + C_{Mx\beta}\beta + (C_{Mxr} - C_{Mx\dot{\beta}})r \\ C_{Mz} &= C_{Mz0} + C_{Mz\beta}\beta + (C_{Mzr} - C_{Mz\dot{\beta}})r \end{aligned} \quad (5)$$

Likewise for a forced oscillation in roll direction, the aerodynamic coefficients are written as:

$$\begin{aligned} C_Y &= C_{Y0} + C_{Y\beta}\beta + C_{Yp}p \\ C_{Mx} &= C_{Mx0} + C_{Mx\beta}\beta + C_{Mxp}p \\ C_{Mz} &= C_{Mz0} + C_{Mz\beta}\beta + C_{Mzp}p \end{aligned} \quad (6)$$

Note that the sideslip angle of $\beta(t)$ is related to the bank angle of $\phi(t)$ as:

$$\beta(t) = -\sin^{-1}(\sin\alpha \sin\phi(t)) \quad (7)$$

The coefficients in front of each input parameter are called stability derivatives and should be estimated. Two different estimation methods are used in this work, linear regression method and a method based on points of maximum and minimum angular velocity. These methods are briefly described.

A. Linear Regression Method

Equations 4-7 can be arranged in the form of:

$$y = \beta_0 + \beta_1 x_1 + \beta_2 x_2 + \dots + \beta_k x_k + \epsilon \quad (8)$$

where y is a chosen aerodynamic coefficient; x_1, x_2, \dots, x_k are corresponding inputs; $\vec{\beta} = [\beta_0, \beta_1, \dots, \beta_k]$ is the vector of unknown coefficients for selected aerodynamic coefficient and ϵ is the approximation error. Now assume there are n samples of function of y ; define the vectors of $\vec{y} = [y_1, y_2, \dots, y_n]$ and $\vec{\epsilon} = [\epsilon_1, \epsilon_2, \dots, \epsilon_n]$; In this work \vec{y} contains full CFD data from forced oscillation motions and n is number of time steps. Independent inputs of x_1, x_2, \dots, x_k are the variables used in Eqs. 4-7 (e.g. α, β, \dots). These variables are known at each time step of motion. The input matrix of X is then defined as:

$$\mathbf{X} = \begin{bmatrix} 1 & x_{11} & \cdots & x_{k1} \\ 1 & x_{12} & \cdots & x_{k2} \\ \vdots & \vdots & \ddots & \vdots \\ 1 & x_{1n} & \cdots & x_{kn} \end{bmatrix} \quad (9)$$

The sum of squared errors should be minimized; the squared error is:

$$S = (\vec{y} - X^T \vec{\beta})^T (\vec{y} - X^T \vec{\beta}) \quad (10)$$

The unknown parameters can then be estimated as:

$$\vec{\beta} = (X X^T)^{-1} (X \vec{y}) \quad (11)$$

B. Points of Maximum and Minimum Angular Velocity

This is a very simple method for direct calculation of dynamic derivatives (combined terms) from simulations of forced periodic motions. Consider the pitch moment changes during a sinusoidal pitching motion

$$C_{My} = C_{My_0} + C_{My_\alpha}(\alpha - \alpha_0) + (C_{My_{\dot{\alpha}}} + C_{My_q})q \quad (12)$$

The plot of pitch moment versus angle of attack makes a quasi-steady elliptical hysteresis as illustrated in Fig. 2. There exists two points at which the angular velocity is maximum and minimum. These points are where $\alpha = \alpha_0$ as shown in Fig. 2. The maximum and minimum angular velocities equal to $+\omega A$ rad/s and $-\omega A$ rad/s. Denote pitch moment values at these points as C_{m+} and C_{m-} and substitute them in Eq. 12 to find below equations:

$$\begin{aligned} C_{m+} &= C_{My_0} + (C_{My_{\dot{\alpha}}} + C_{My_q}) \frac{\omega A c}{2V} \\ C_{m-} &= C_{My_0} - (C_{My_{\dot{\alpha}}} + C_{My_q}) \frac{\omega A c}{2V} \end{aligned} \quad (13)$$

If we subtract these equations, the pitch damping moment can be found as:

$$C_{My_{\dot{\alpha}}} + C_{My_q} = \frac{C_{m+} - C_{m-}}{2kA} \quad (14)$$

where $k = \frac{\omega c}{2V}$ is the reduced frequency. Other damping coefficients can be estimated in a similar fashion.

III. Flow Solvers

Cobalt and Kestrel flow solvers are used in this work. Both codes originated from the Air Vehicles Unstructured Solver (AVUS, formally known as Cobalt60) that was developed at the Air Force Research Laboratory (AFRL).^{13,14} Cobalt is now a commercial code whilst Kestrel is being developed by the U.S. Department of Defense as part of the CREATETM-AV program. More details are given below:

A. Cobalt Solver

The Cobalt code¹⁴ solves the unsteady, three-dimensional and compressible Navier-Stokes equations in an inertial reference frame. The ideal gas law and Sutherland's law close the system of equations and the entire equation set is nondimensionalized by free stream density and speed of sound.¹⁴ The Navier-Stokes equations are discretised on arbitrary grid topologies using a cell-centered finite volume method. Second-order accuracy in space is achieved using the exact Riemann solver of Gottlieb and Groth,¹⁵ and least squares gradient calculations using QR factorization. To accelerate the solution of discretized system, a point-implicit method using analytic first-order inviscid and viscous Jacobians. A Newtonian sub-iteration method is used to improve time accuracy of the point-implicit method. Tomaro et al.¹⁶ converted the code from explicit to implicit, enabling Courant-Friedrichs-Lewy numbers as high as 10^6 . Some available turbulence models for Reynolds-averaged Navier-Stokes (RANS) and delayed detached-eddy simulations (DDES) are the Spalart-Allmaras model,¹⁷ Wilcox's $k-\omega$ model,¹⁸ and Mentor's SST model.¹⁹

B. Kestrel Solver

Kestrel is a new DoD-developed CFD solver in the framework of CREATE Program which is funded by the High Performance Computing Modernization Program (HPCMP). The CREATE™ Program is a 12-year program, started in 2008, and is aimed at addressing the complexity of applying computationally based engineering to improve DoD acquisition processes.²⁰ CREATE™ consists of three computationally based engineering tool sets for design of air vehicles, ships, and radio-frequency antennae. The fixed wing analysis code, Kestrel, is part of the Air Vehicles Project (CREATE™-AV) and is a modularized, multidisciplinary, virtual aircraft simulation tool incorporating aerodynamics, structural dynamics, kinematics, and kinetics.²⁰

The flow solver component of Kestrel (named kCFD) solves the unsteady, three-dimensional, compressible RANS equations on hybrid unstructured grids.²¹ Its foundation is based on Godunov's first-order accurate, exact Riemann solver.²² Second-order spatial accuracy is obtained through a least squares reconstruction. The code also uses an implicit Newton sub-iteration method to improve time accuracy as well. Grismer et al¹³ parallelized the code, with a demonstrated linear speed-up on thousands of processors. Kestrel receives an eXtensible Markup Language (XML) input file generated by Kestrel User Interface and stores the solution convergence and volume results in a common data structure for later use by the Output Manager component. Some available turbulence models are the Spalart-Allmaras model, Spalart-Allmaras rotation correction (SARC), and DDES with SARC.

IV. Test Cases

The details of test cases can be found in Ref. 11. Briefly, four wings are studied. These wings have either an open or closed inlet and are with and without a left-side bending trailing edge. TE deflection is approximately 45° as measured from the flat lower surface. These wings are named *SR*, *BR*, *OpenS* and *OpenB* representing straight/round, bent/round, open/straight, and open/bent geometries.

The airfoil section of all wings were provided by NSRDEC and was based on a modified Clark-Y with a flat lower surface used as the cut pattern for drop tested systems.²³ The wing planform is characterized by a rectangular wing with an aspect ratio of two and zero anhedral angle. The open wings have fourteen cells as well.

viscous grids are generated for the full-geometry wings. These grids are unstructured with prismatic layers near the surfaces. Inviscid tetrahedral grids were generated by the ICEM-CFD code; these grids were then used as a background grid by the grid generator of TRITET^{24,25} which builds prism layers using a frontal technique. TRITET rebuilds the viscous grid while respecting the size of the original inviscid grid from ICEM-CFD. The closed-wing grids have around 30 million cells and the open-wing grids contain about 45 million cells. The surface grids are shown in Fig. 3. Note that grids have a left-side bending, however, the pictures of Fig. 3 are the mirror images to show the bent side and open inlets.

The static experiments of closed wings were performed in the subsonic wind tunnel of USAFA. This closed-loop tunnel has an 8 ft long test section with a test section cross-section 3 ft by 3 ft. The tunnel can achieve speeds in excess of Mach 0.5. Bergeron et al.²³ detailed the experimental setup and data of ram-air parachutes. The experimental Mach and Reynolds number were 0.25 and 1.4×10^6 . The lift and drag forces and pitch moment coefficients were measured by an external force balance installed under the wind tunnel.

V. Results and Discussion

All CFD simulations were run on the Air Force Research Laboratory (AFRL) machines of Spirit and Thunder with core speeds of 2.6 and 2.3 GHz. Standard viscous no-slip wall boundary conditions are used for the solid surfaces, with a farfield boundary condition on the outer sphere. The flow conditions and solver setup are identical in Cobalt and Kestrel flow solvers.

Closed wing simulations were performed using the SST turbulence model and ran for 2,000 time steps. Open wings ran for 6,000 time steps and used the SARC-DDES turbulence model to capture the separation bubble(s) forming and collapsing near the leading edge. Static simulations are unsteady with second order spatial and temporal accuracy. Time step value was set to 1×10^{-4} second, and two Newton sub-iterations were used. Dynamic motion runs were made with five Newton sub-iterations to improve time accuracy of the point implicit method and approximate Jacobians. In all simulations, the free-stream Mach number is 0.25 and the Reynolds number corresponds to 1.4 million to match experimental conditions. The moment reference point and the point of rotation are at the wing's quarter chord.

The validation results are described first. After 2,000 time steps, the coefficient of closed wings in CFD reached a constant value. Figure 4 compares predictions with the experimental data of closed wings. In this figure, Kestrel and Cobalt predictions are shown as solid and dashed-dot lines, respectively. Very good agreement is observed in all coefficients between predictions of Cobalt and Kestrel. However, the stall behaviors do not match up. Cobalt predicts a stall around 16° , but no stall was observed in Kestrel. Figure 4 shows the preliminary experimental data from wind tunnel as well. The measurements before stall agree very well with the predictions as seen in Fig. 4. Based on these experiments, Cobalt may have predicted the stall angle correctly. Figure 4 also shows that by pulling the trailing edge down the lift coefficient increases but the lift curve slope remains constant. The drag increases for the bent geometry as well. The pitch moment about the wing's quarter point becomes more negative. The left-side bending will produce a negative side-force, a positive roll and a negative yaw moment as well. Finally, these wings have a large positive camber and therefore produce some lift at zero angle of attack. The pitch moment about the quarter chord is nearly constant.

The open wing simulations ran for 6,000 time steps, but some CFD solutions still show coefficient variations at final time steps. Therefore, the solutions at last 500 time steps were averaged to obtain the mean values. Computed and measured aerodynamic coefficients of open wings are shown in Fig. 5. Notice that only the straight wing was tested in the wind tunnel. Figure 5 shows that again Cobalt and Kestrel computations reasonably match each other and experiments before stall. At some conditions, Kestrel may outperform Cobalt predictions. Compared with closed wings, opening the leading edge will increase the drag. The lift coefficient will stall earlier. The pitch moment curve slope will become negative. The aerodynamic nonlinearity can be seen in Fig. 5 even at small angles of attack

After validation for CFD results, the stability derivatives are calculated by imposing a forced sinusoidal motion around the wing's quarter point. The first motions considered are pitching oscillation with an amplitude of one degree and a reduced frequency of 0.1 starting at different angles of attack up to 10° . Figure 6(a)-(b) show computed lift and pitch moment loops of the *SR* wing for oscillations about a mean angle of six degrees using Cobalt and Kestrel. The loop directions from both codes match each other; Kestrel, however, forms slightly thinner loops. The lift loops are circumvented in a clockwise direction; but counter-clockwise loops are seen for the pitch moment. Both estimation methods were used to calculate stability derivatives of the *SR* wing from these full CFD simulations. The results of the linear regression method are shown with solid lines in Fig. 6; the pitch damping derivatives are found from the points of maximum and minimum angular velocity and are shown with dashed-dot lines in Figs. 6 (e)-(f). Both methods produced very similar result. Figure 6 shows that *SR* wing has nearly constant slope curve values with the angle of attack. Pitch moment curve slope is near zero. This wing geometry has damping derivatives that remained nearly constant with angle of attack as well. Kestrel data result in smaller damping force and less negative damping moment compared with Cobalt.

Next results present the effects of reduced frequency on calculated stability derivatives of the *SR* wing. Two sets of motions were generated for reduced frequencies of $k = 0.1$ and $k = 0.05$. All motions have one degree amplitude and start at different angles of attack. These motions were simulated in Cobalt. Figure 7 compares the hysteresis loops of both motions with six degrees mean angle of attack. As the reduced frequency increases, the hysteresis effect becomes larger as seen in Fig. 7. Stability derivatives are calculated using linear regression method and are shown in Fig. 7 for both motions. Some variations can be seen in derivatives due to reduced frequency changes, but they are small.

The open wing stability derivatives were calculated from pitching harmonic motions and are compared with those found for the SR wing in Fig. 8. CFD data shown in the figure are Cobalt predictions. Motions again have one degree amplitude and have reduced frequencies of 0.1 and 0.05. Derivatives were calculated using the linear regression model and the method based on maximum/minimum angular velocity. The lift and pitch moment hysteresis loops at $\alpha = 6^\circ$ can be seen in Figs. 8 (a)-(b). These loops are very different from those found for the closed wing. At $\alpha = 6^\circ$, the hysteresis loops of the open wing are thinner and have different directions. Curve slopes of the open wing show significant changes with angle of attack as seen in Figs. 8 (c)-(d). The pitch moment slope of the open wing is non zero and has negative values. Figures 8 (e)-(f) show that both methods produce similar results, in particular for the angle of attack ranging from four to eight degrees. Pitch damping derivatives of the open wing change significantly with the angle of attack. As detailed in Ref. 23, the open wings have an eddy formed over the lower surface at small angles of attack. The eddy becomes smaller with increasing angle of attack. At higher angles, the flow separates at the upper surface as well. These features make aerodynamics of the open wings very nonlinear. The effects of motion reduced frequency on damping derivatives can be seen in Figs. 8 (e)-(f). The derivatives become frequency-dependent at high angles of attack.

Yaw damping derivatives of the closed wing are calculated from periodic yawing motions and shown in Fig. 9. The motions again have one degree sideslip amplitude and have a reduced frequency of 0.1. Referring to Eqs. 5 and 6, the derivatives with respect to sideslip angle can be found from both yawing and rolling motions. Figure 9 compares calculated derivatives from both motions at different angles of attack. Yawing-motion derivatives are shown with solid lines; the dashed-dot lines correspond to rolling-motion derivatives. Note that during the rolling motion, the sideslip angle is related to the bank angle and the angle of attack, such that it increases with increasing the angle of attack. Figure 9 shows that calculated derivatives are different using rolling and yawing motions; they become closer as the angle of attack increases. Results of Fig. 9 confirm that Cobalt and Kestrel predictions are very similar for the closed wing geometry. Finally, the stability derivatives shown in Fig. 9 slightly change with angle of attack.

Next, the closed and open wing stability derivative during the yawing motions are compared with each other in Fig. 10. All simulations were obtained using Cobalt. The closed wing derivatives change smooth and small with the angle of attack. However, the open wing derivatives are very sensitive to changes in the angle-of-attack. Figure 10 shows that at about 7 to 8 degrees angle of attack, the open and closed wing derivatives are closer. At these angles, a much smaller eddy is formed on the lower surface. This eddy is probably the cause of large changes seen at small angles.

Aerodynamic derivatives with respect to rolling motions are shown in Fig. 11 for the open and closed wings. In these motions, the grids rotate about the x axis with a reduced frequency of 0.1 and one degree amplitude. Figure 11 shows that the open wing has again a nonlinear behavior even at small angles of attack.

Damping derivatives during pitching and yawing motions have the effects of both angular velocity and unsteady effects ($\dot{\alpha}, \dot{\beta}$). To separate these effects, periodic translation motions might be used. In these motions, the angular velocities are zero and the hysteresis loops are due to unsteady effects. To demonstrate the method, a plunging motion was applied to the open and closed wings. The motion inputs include α and $\dot{\alpha}$ but not the pitch rate. The maximum displacement was selected such that the effective angle of attack changes from -1 to 1 around the mean angle of attack. Stability derivatives are calculated from plunging motions and are compared with those found from the pitching motions in Fig. 12. The comparisons show that for these wings, $\dot{\alpha}$ effects are the largest factor for pitch damping derivatives.

Since the stability derivatives are found they can be used for aerodynamic predictions of new motions. In this work, the stability derivatives models are tested for a chirp motion. The chirp motion used has a constant amplitude and linearly increasing frequency in time. The motion is shown in Fig. 13 (a). The model predictions based on stability derivatives are compared with the full CFD data in Fig. 13. To show the motion effects, the static data are also included in the plots. The comparisons show a good agreement between model and full CFD data for the closed wings. Static data only depend on the current angle of attack and do not change with angular velocity. Figure 13 (d) shows that the static data underestimate the model and CFD data for the pitch moment. There are some lag effects between static and full CFD data as well. For the open wings, the models do not match CFD everywhere. The comparison results show that CFD data of the open wings are time dependent. For example, Fig. 13 (d) depicts that maximum pitch moment coefficient obtained in CFD can increase and decrease as time progresses, although frequency does increase in time. These results suggest substantial unsteady effects present on the numerical simulations of open wings during the motion. These effects cannot be reconciled with stability derivatives.

VI. Concluding Remarks

This work concentrated on calculating and evaluating the stability derivative for the aerodynamic predictions of ram-air parachutes with open and closed inlets. All wings were assumed to be rigid and have an aspect ratio of two. Aerodynamic predictions were made with flow solvers of Cobalt and Kestrel and were compared with available wind-tunnel experimental data. Simulations and measurements were carried out at a Mach number of 0.25 and Reynolds number of 1.4 million.

The results showed that experimental data of wings considered here match the computational predictions quite well. The calculated derivatives were similar for both methods and showed only a small change with reduced frequencies less than 0.1. The results showed that damping derivatives of closed wings remain fairly constant up to ten degrees angle of attack. However, the open wings showed a very sensitive behavior in damping derivatives with respect to angles of attack. The models were evaluated for the closed and open wings undergoing a chirp motion of increasing frequency. The results of the comparison showed that the aerodynamic models of the closed wing match time-marching full CFD calculations well, but some discrepancies were seen in the open wing plots. These results suggested substantial unsteady effects present on the numerical simulations of open wings during the motion. These effects cannot be reconciled with stability derivatives.

VII. Acknowledgements

Mehdi Ghoreyshi is supported by USAFA; their financial support is gratefully acknowledged. Acknowledgements are expressed to the Department of Defense High Performance Computing Modernization Program (HPCMP) and AFRL for providing computer time. The authors appreciate the support provided by NSRDEC Airdrop Technology Team and the High Performance Computing Research Center at USAFA.

References

- ¹Force Multiplying Technologies for Logistics Support to Military Operations, National Academies Press, 2014.
- ²Carter, D., Singh, L., Wholey, L., Rasmussen, S., Barrows, T., George, S., McConley, M., Gibson, C., Tavan, S., and Bagdonovich, B., "Band-Limited Guidance and Control of Large Parafoils," AIAA Paper 2009-2981, May 2009.
- ³Benney, R. J., Krainski, W. J., Onckelinx, C. P., Delwarde, C. C., Mueller, L., and Vallance, M., "NATO Precision Airdrop Initiatives and Modeling and Simulation Needs," RTO-MP-AVT-133 Technical Report, October 2006.
- ⁴Harrington, N. and Doucette, E., "Army After Next and Precision Airdrop," *Army Logistician*, Vol. 31, No. 1, 1999, pp. 46.
- ⁵Mittal, S., Saxena, I. P., and Singh, A., "Computation of Two-Dimensional Flows Past Ram-Air Parachutes," *International Journal For Numerical Methods in Fluids*, Vol. 35, 2001, pp. 643-667.
- ⁶Lingard, J. S., "Precision Aerial Delivery Seminar Ram-Air Parachute Design," 13th AIAA Aerodynamic Decelerator Systems Technology Conference, Clearwater Beach, May 1995.
- ⁷Lingard, J. S., "The Aerodynamics of Gliding Parachute," 9th AIAA Aerodynamic Decelerator Systems Technology Conference, AIAA Paper 1986-2427, May 1986.
- ⁸Mohammadi, M. A. and Johari, H., "Computations of Flow Over a High Performance Parafoil," AIAA Paper 2009-2972, May 2009.
- ⁹Ghoreyshi, M., Seidel, J., Bergeron, K., Lofthouse, A. J., and Cummings, R. M., "Grid Quality and Resolution Effects on the Aerodynamic Modeling of Parachute Canopies," AIAA Paper 2015-0407, January 2015.
- ¹⁰Ghoreyshi, M., Seidel, J., Bergeron, K., Jirasek, A., Lofthouse, A. J., and Cummings, R. M., "Prediction of Aerodynamic Characteristics of a Ram-Air Parachute," AIAA Paper 2014-2831, June 2014.
- ¹¹Ghoreyshi, M., Bergeron, K., Jirasek, A., Seidel, J., Lofthouse, A. J., and Cummings, R. M., "Computational Aerodynamic Modeling For Flight Dynamics Simulation of Ram-Air Parachutes," AIAA Paper 2015-3169, June 2015.
- ¹²Da Ronch, A., Vallespin, D., Ghoreyshi, M., and Badcock, K. J., "Evaluation of Dynamic Derivatives Using Computational Fluid Dynamics," AIAA Journal, 2012.
- ¹³Grismer, M. J., Strang, W. Z., Tomaro, R. F., and Witzeman, F. C., "Cobalt: A Parallel, Implicit, Unstructured Euler/Navier-Stokes Solver," *Advanced Engineering Software*, Vol. 29, No. 3-6, 1998, pp. 365-373.
- ¹⁴Strang, W. Z., Tomaro, R. F., and Grismer, M. J., "The Defining Methods of Cobalt: A Parallel, Implicit, Unstructured Euler/Navier-Stokes Flow Solver," AIAA Paper 1999-0786, 1999.
- ¹⁵Gottlieb, J. J. and Groth, C. P. T., "Assessment of Riemann Solvers For Unsteady One-dimensional Inviscid Flows of Perfect Gasses," *Journal of Fluids and Structure*, Vol. 78, No. 2, 1998, pp. 437-458.
- ¹⁶Tomaro, R. F., Strang, W. Z., and Sankar, L. N., "An Implicit Algorithm For Solving Time Dependent Flows on Unstructured Grids," AIAA Paper 1997-0333, 1997.
- ¹⁷Spalart, P. R. and Allmaras, S. R., "A One Equation Turbulence Model for Aerodynamic Flows," AIAA Paper 1992-0439, January 1992.

¹⁸Wilcox, D. C., "Reassessment of the Scale Determining Equation for Advanced Turbulence Models," *AIAA Journal*, Vol. 26, November, 1988, pp. 1299–1310.

¹⁹Menter, F., "Eddy Viscosity Transport Equations and Their Relation to the $k - \varepsilon$ Model," *ASME Journal of Fluids Engineering*, Vol. 119, 1997, pp. 876–884.

²⁰Roth, G. L., Morton, S. A., and Brooks, G. P., "Integrating CREATE-AV Products DaVinci and Kestrel: Experiences and Lessons Learned," AIAA Paper 2012-1063, January 2012.

²¹Morton, S. A., McDaniel, D. R., Sears, D. R., Tillman, B., and Tuckey, T. R., "Kestrel: A Fixed Wing Virtual Aircraft Product of the CREATE Program," AIAA Paper 2009-0338, January 2009.

²²Godunov, S. K., "A Difference Scheme for Numerical Computation of Discontinuous Solution of Hydrodynamic Equations," *Sbornik Mathematics*, Vol. 47, 1959, pp. 271–306.

²³Bergeron, K., Jurgen, S., and McLaughlin, T., "Wind Tunnel Investigations of Rigid Ram-Air Parachute Canopy Configurations," AIAA Paper 2015-2156, March-April 2015.

²⁴Tyssel, L., "Hybrid Grid Generation for Complex 3D Geometries," Proceedings of the 7th International Conference on Numerical Grid Generation in Computational Field Simulation, 2000, pp. 337–346.

²⁵Tyssel, L., "The TRITET Grid Generation System," International Society of Grid Generation (ISGG)," Proceedings of the 10th International Conference on Numerical Grid Generation in Computational Field Simulations, 2000.

²⁶Computational Research and Engineering Acquisition Tools And Environments (CREATE), Eglin AFB, FL 32542, *Kestrel User Guide, Version 6.0*, August 2015.

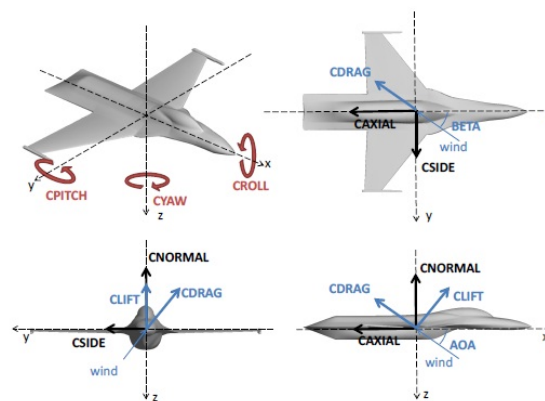


Figure 1. Coordinate system for definition of aerodynamic forces and moments. Adapted from Ref. 26.

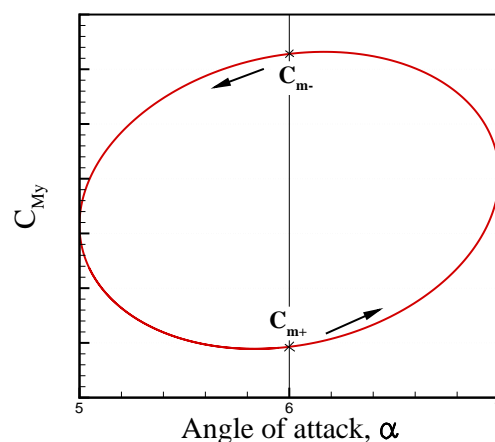
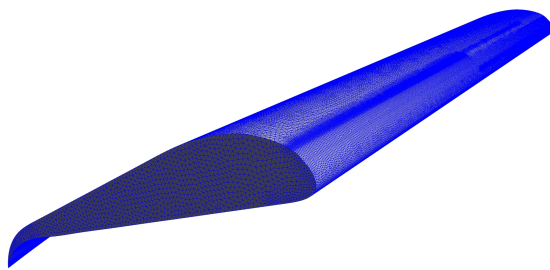
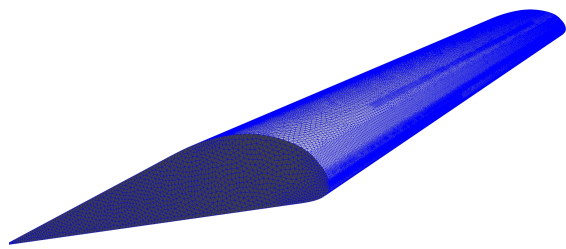


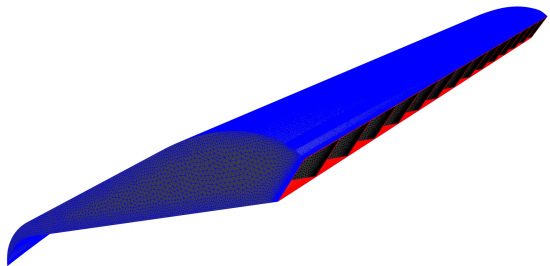
Figure 2. Illustration of a method to identify pitch damping moment from points of maximum and minimum pitch rate.



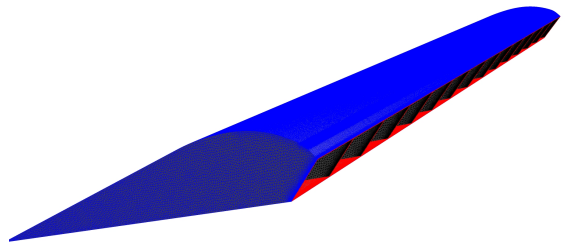
(a) Bent and Round (BR)



(b) Staright and Round (SR)

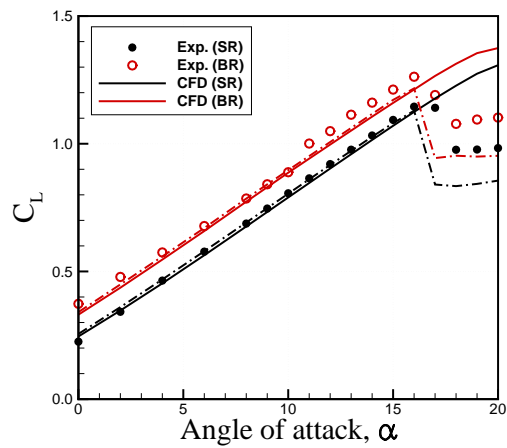


(c) Open and bent

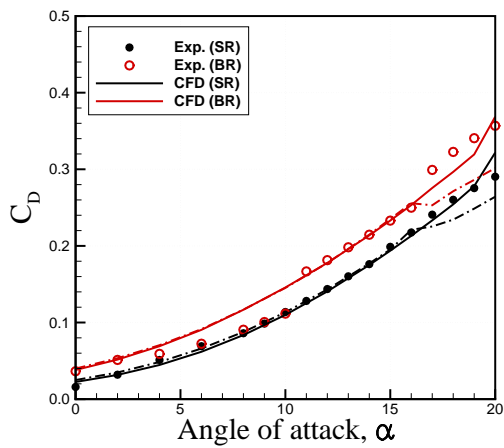


(d) Open and straight

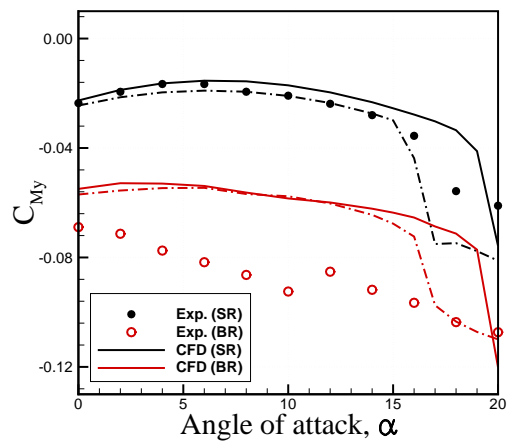
Figure 3. Computational grids.



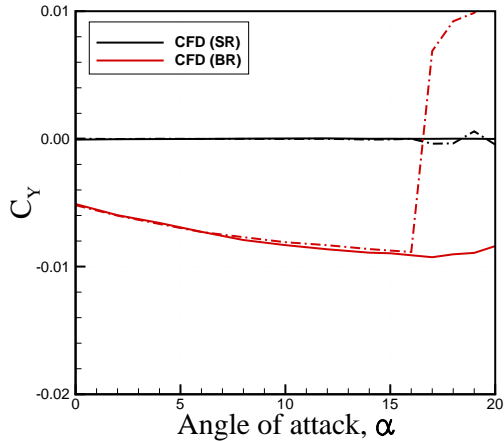
(a) lift coefficient



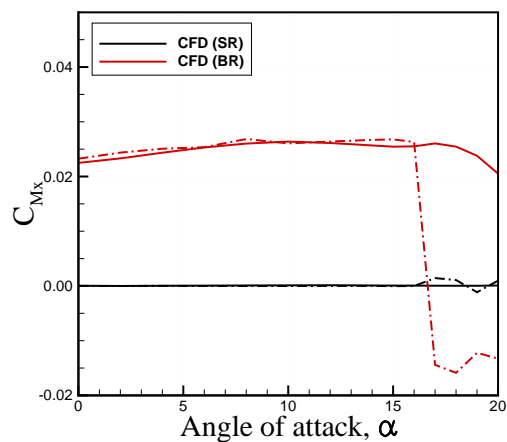
(b) drag coefficient



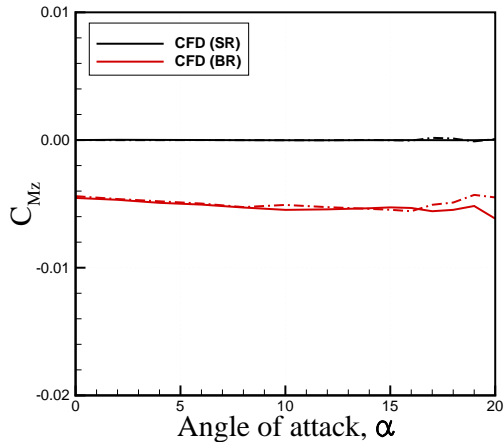
(c) pitch-moment coefficient



(d) side-force coefficient

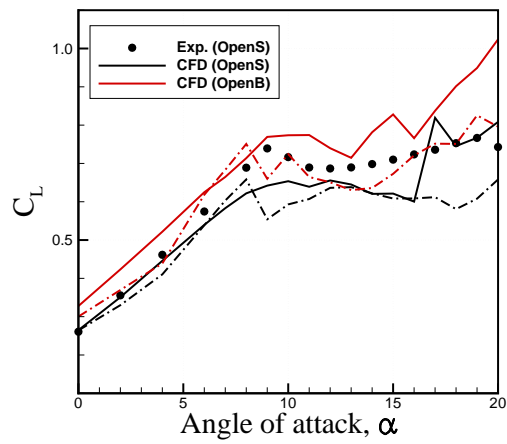


(e) roll-moment coefficient

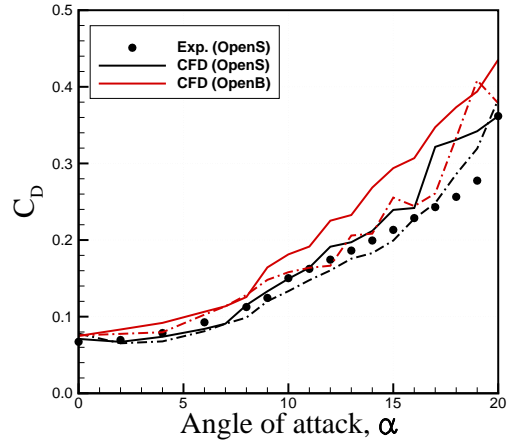


(f) yaw-force coefficient

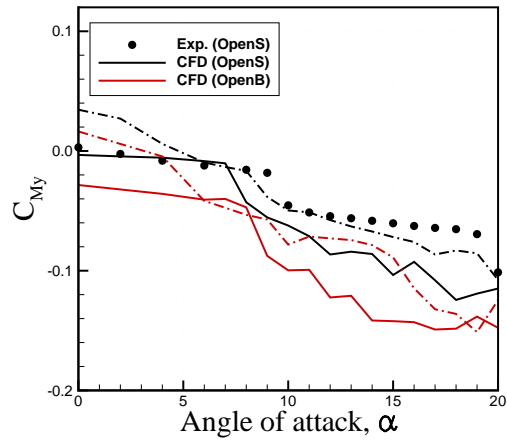
Figure 4. Comparison of aerodynamic predictions of bent/round and straight/round wings using the SST turbulence model.



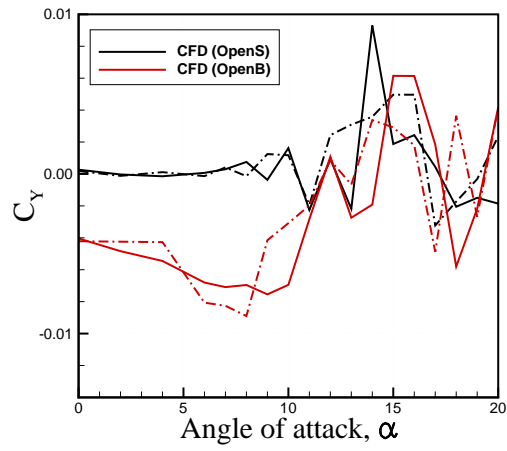
(a) lift coefficient



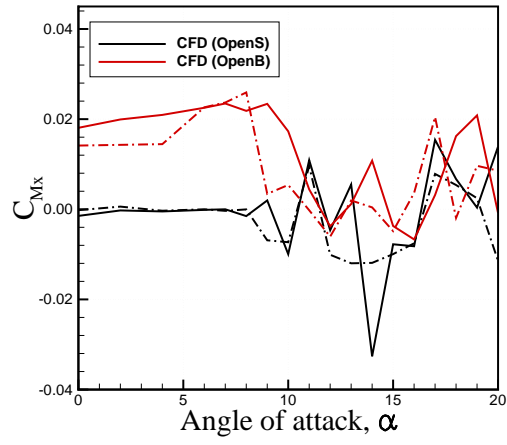
(b) drag coefficient



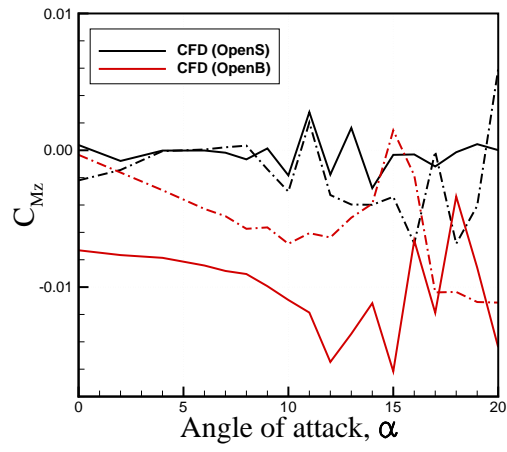
(c) pitch-moment coefficient



(d) side-force coefficient

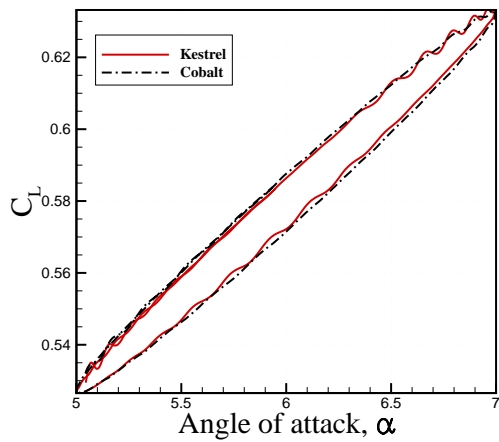


(e) roll-moment coefficient

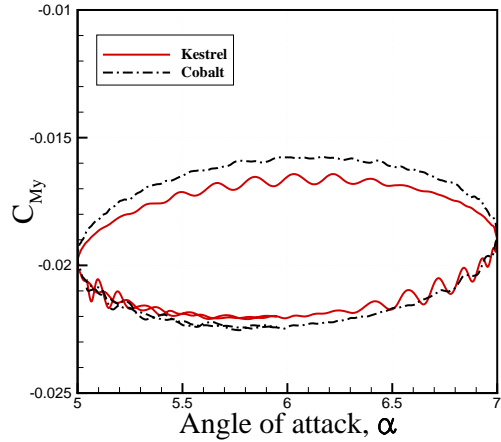


(f) yaw-force coefficient

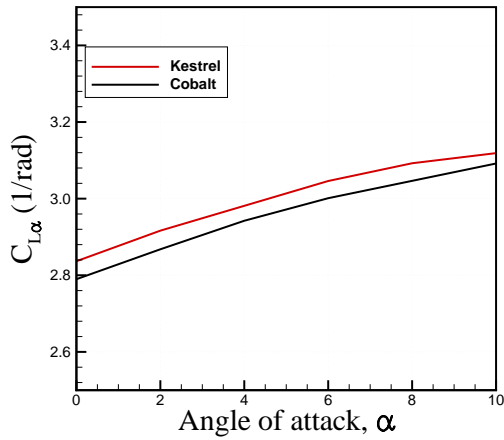
Figure 5. Aerodynamic predictions of open wings.



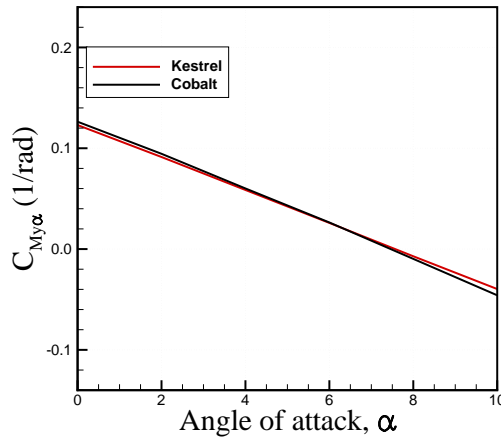
(a) lift coefficient



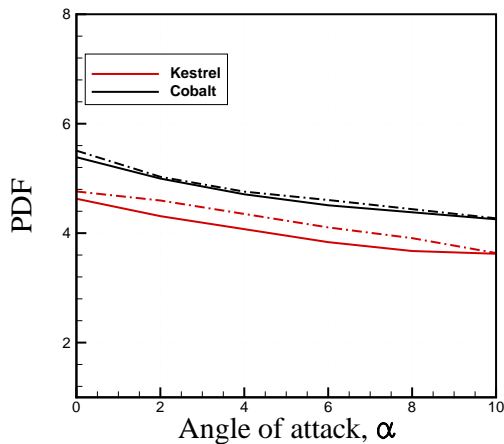
(b) pitch moment coefficient



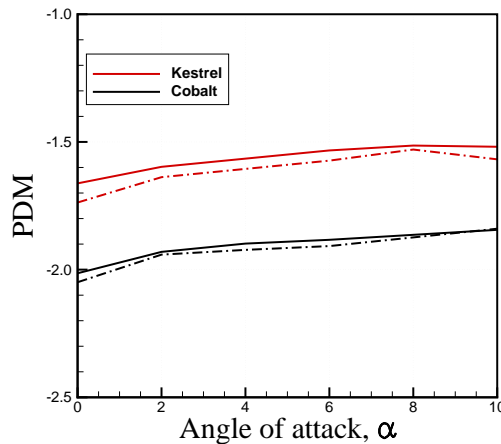
(c) lift curve slope



(d) pitch moment slope

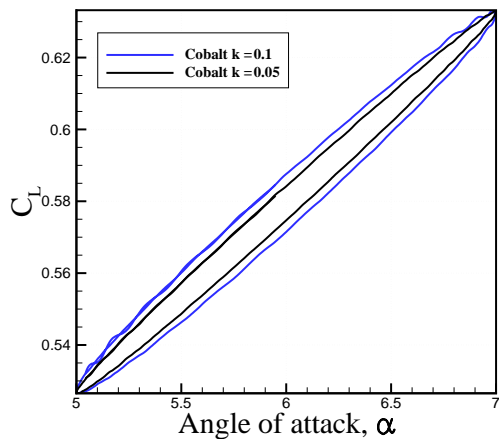


(e) $C_{Lq} + C_{L\dot{\alpha}}$

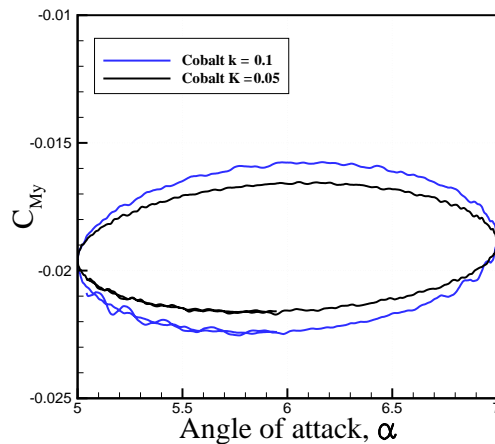


(f) $C_{Myq} + C_{My\dot{\alpha}}$

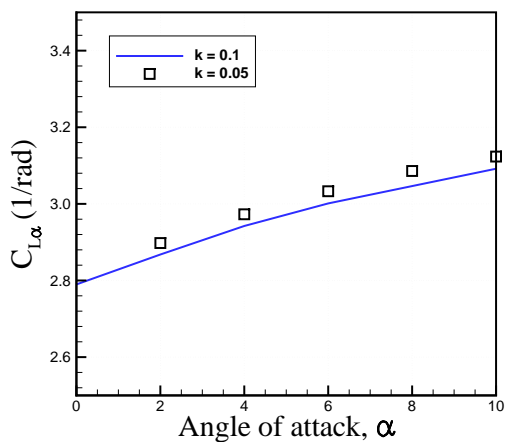
Figure 6. Estimation of longitudinal derivatives for the straight/round wing. Solid and dashed lines correspond to regression and pitch rate methods, respectively.



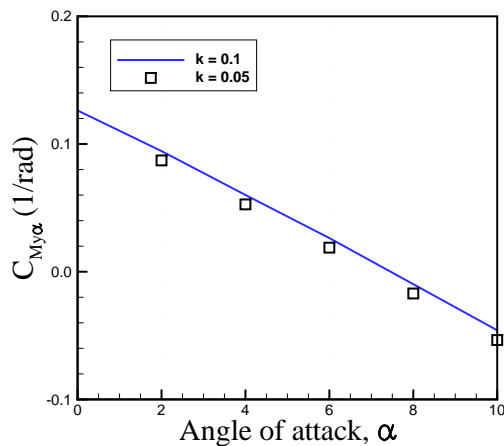
(a) lift coefficient



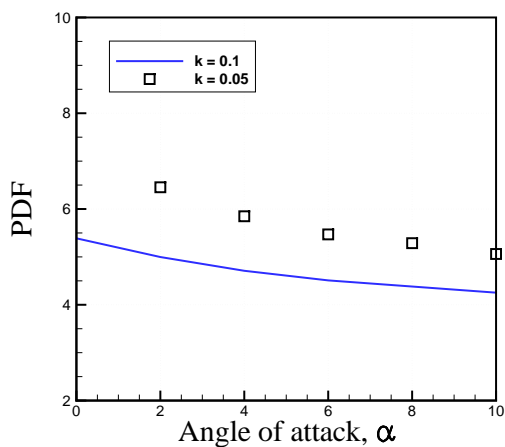
(b) pitch moment coefficient



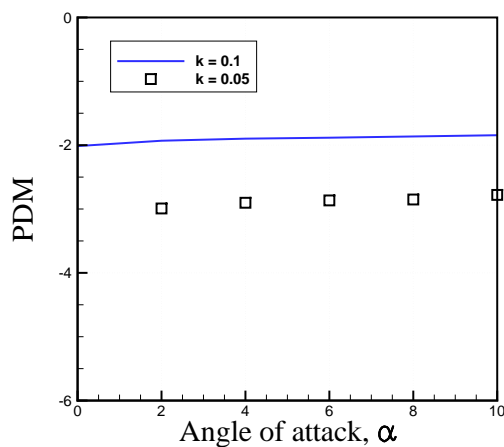
(c) lift curve slope



(d) pitch moment slope

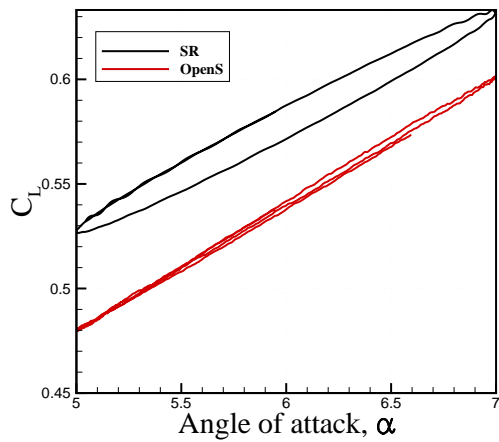


(e) $C_{Lq} + C_{L\dot{\alpha}}$

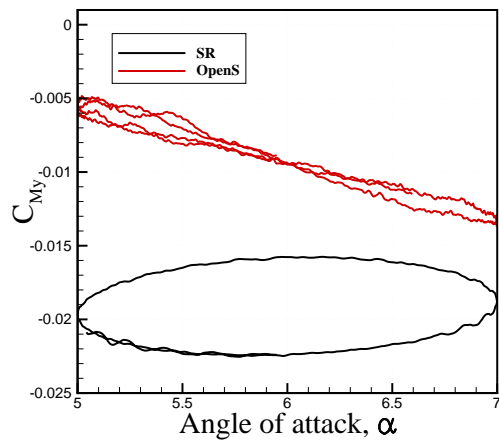


(f) $C_{Myq} + C_{My\dot{\alpha}}$

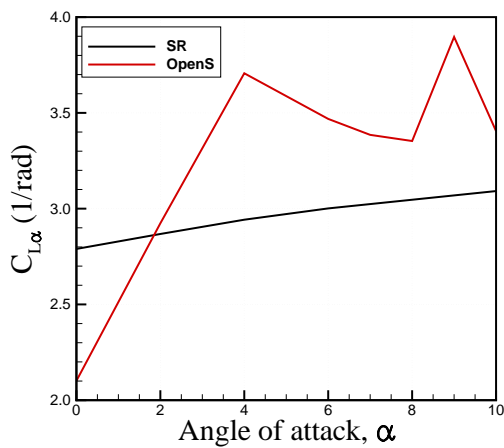
Figure 7. Effects of reduced frequency on pitch damping derivatives.



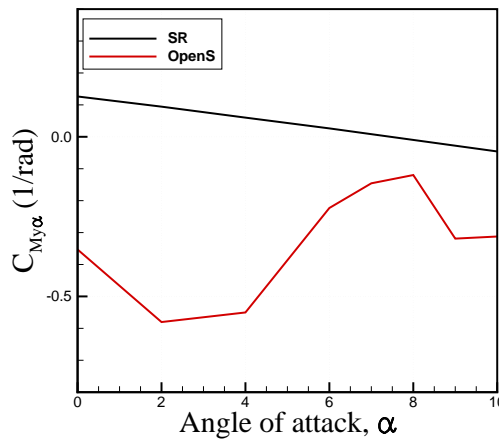
(a) lift coefficient



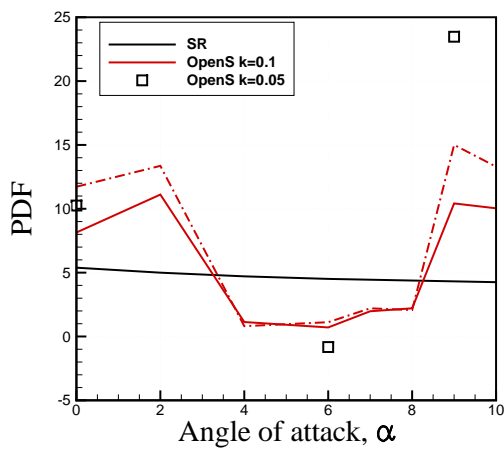
(b) pitch moment coefficient



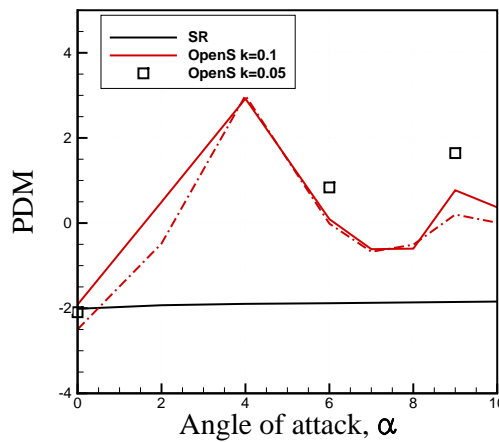
(b) lift curve slope



(c) pitch moment slope

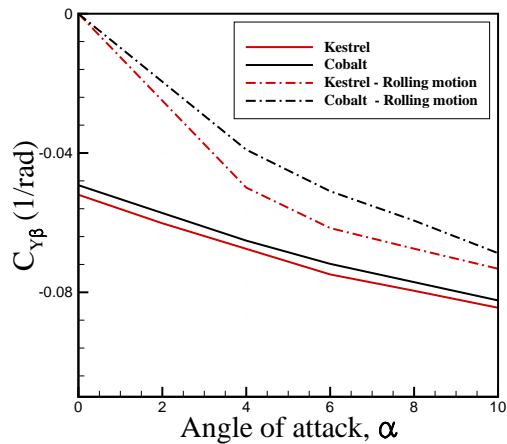


(d) $C_{Lq} + C_{L\dot{\alpha}}$

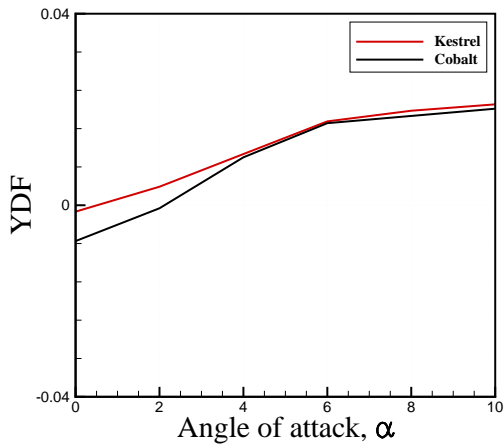


(e) $C_{Myq} + C_{My\dot{\alpha}}$

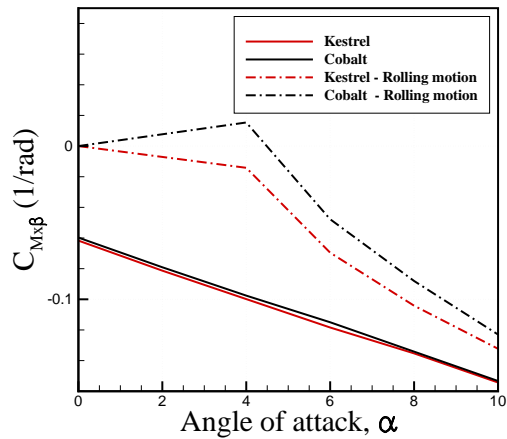
Figure 8. Estimation of longitudinal derivatives for the open straight and straight/round wing. Solid and dashed lines correspond to regression and pitch rate methods, respectively.



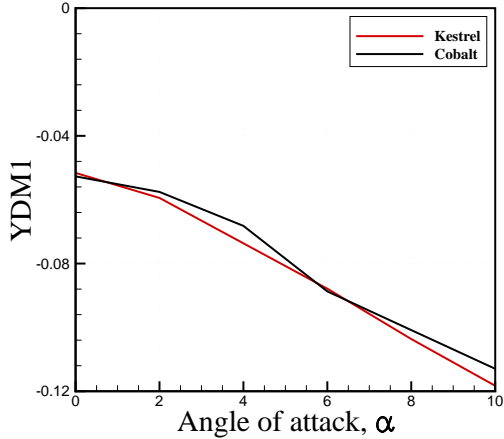
(a) side force curve slope



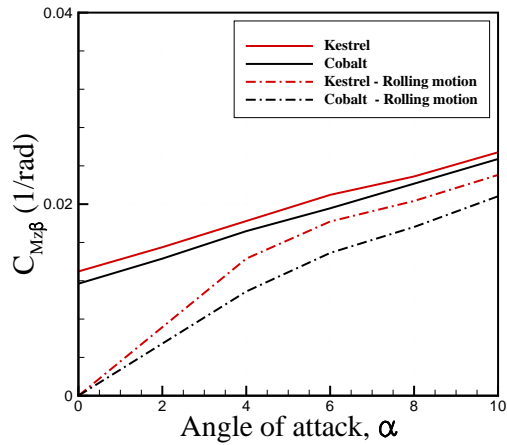
(b) $C_{Yr} - C_{Y\dot{\beta}}$



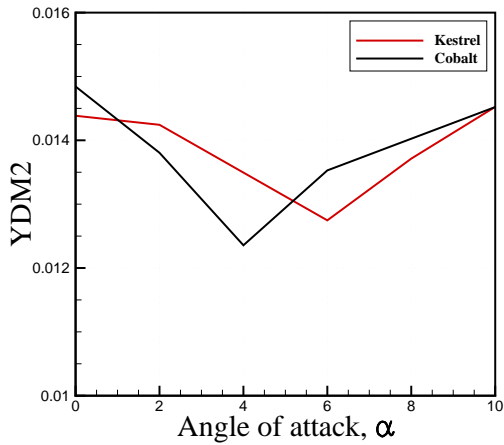
(c) roll moment curve slope



(d) $C_{M_{xr}} - C_{M_{x\dot{\beta}}}$

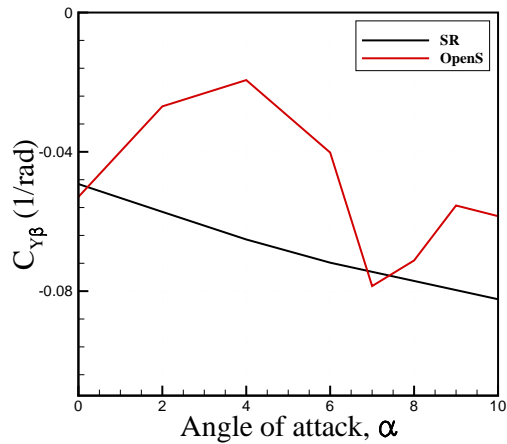


(e) yaw moment curve slope

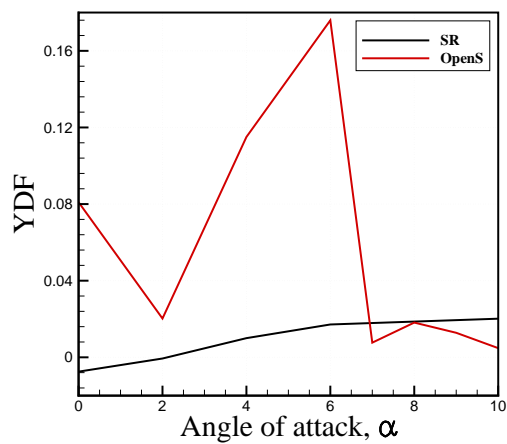


(f) $C_{M_{zr}} - C_{M_{z\dot{\beta}}}$

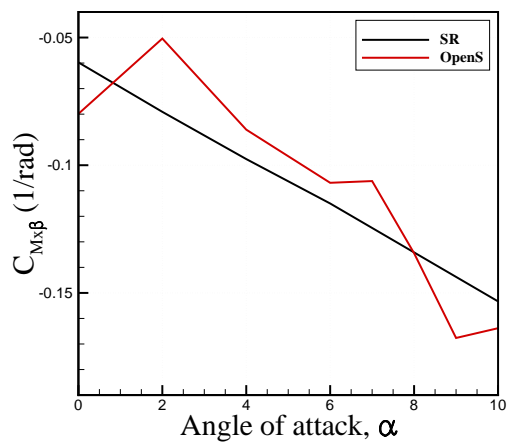
Figure 9. Estimation of yawing derivatives for the closed straight wing.



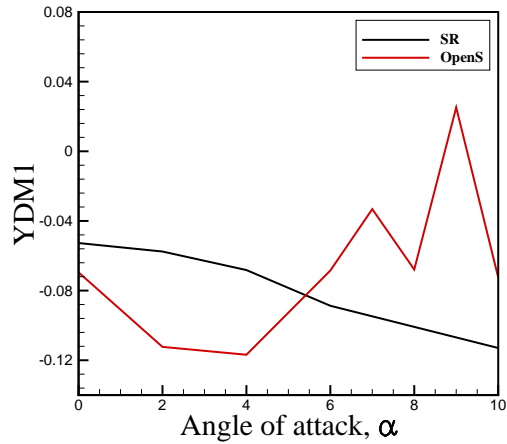
(a) side force curve slope



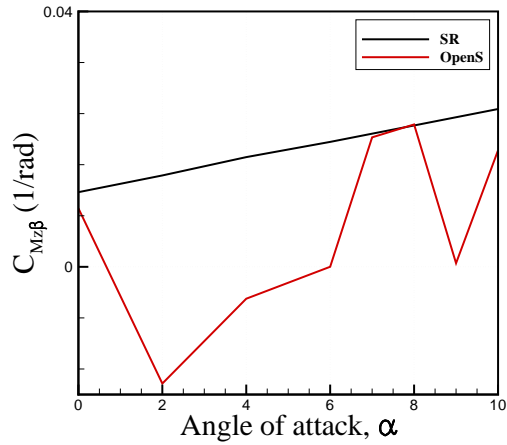
(b) $C_{Yr} - C_{Y\dot{\beta}}$



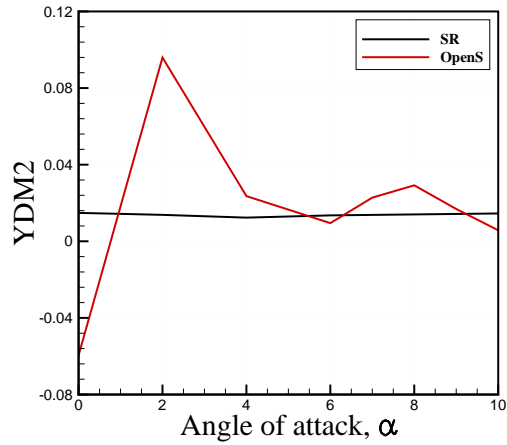
(c) roll moment curve slope



(d) $C_{M_{xr}} - C_{M_{x\dot{\beta}}}$



(e) yaw moment curve slope



(f) $C_{M_{zr}} - C_{M_{z\dot{\beta}}}$

Figure 10. Estimation of yawing derivatives for the open/closed straight wings.

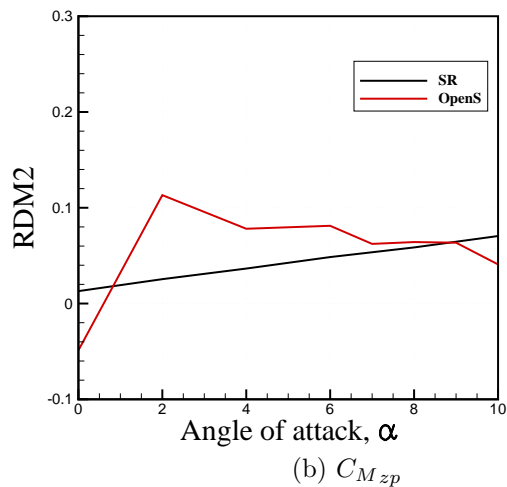
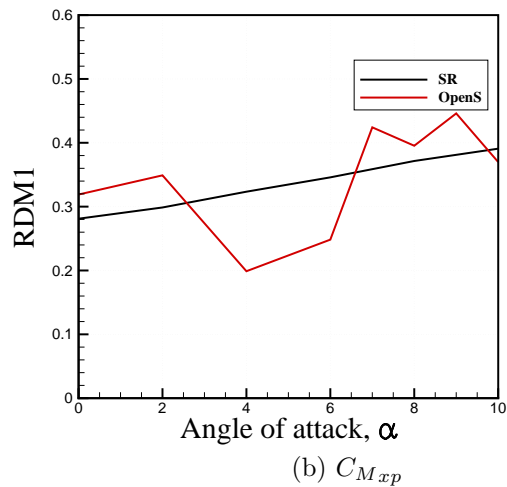
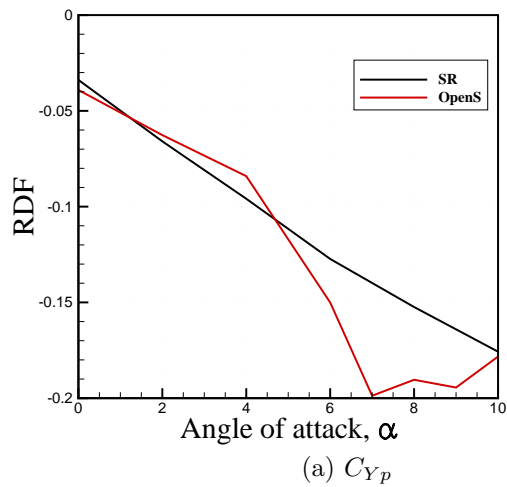
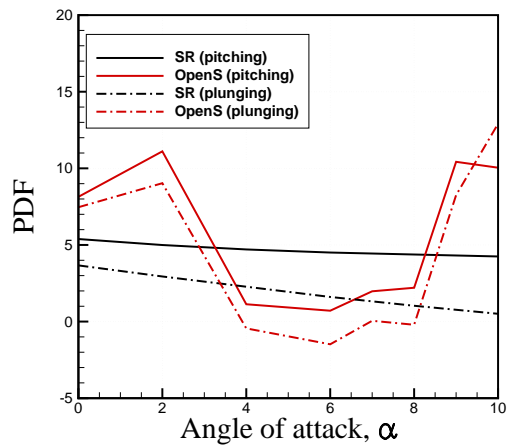
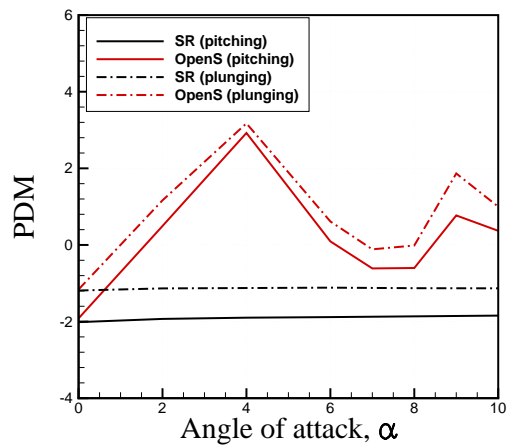


Figure 11. Estimation of rolling derivatives for the open/closed straight wings.

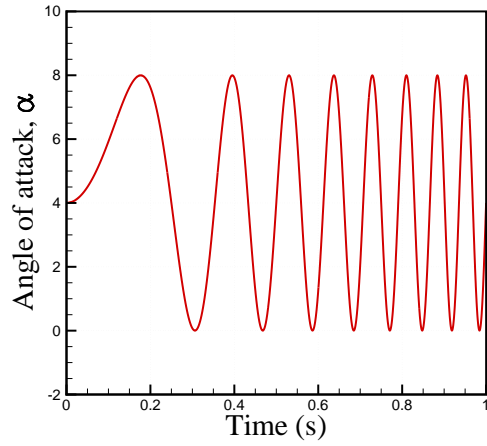


(a) pitching: $C_{Lq} + C_{L\dot{\alpha}}$, plunging: $C_{L\dot{\alpha}}$

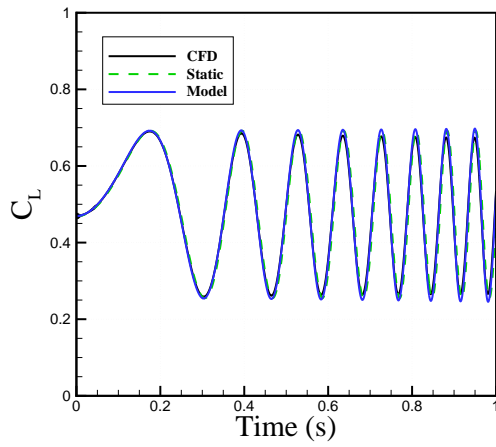


(b) pitching: $C_{M_{yq}} + C_{M_{y\dot{\alpha}}}$, plunging: $C_{M_{y\dot{\alpha}}}$

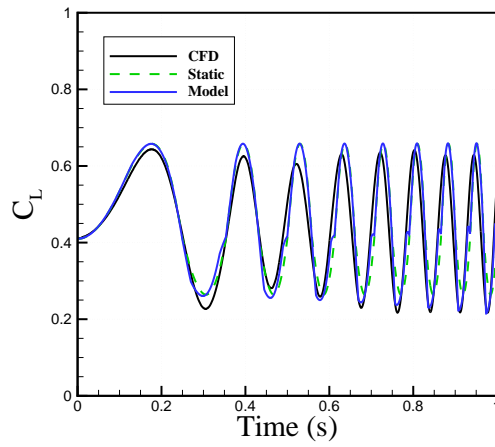
Figure 12. Estimation of pitching derivatives for the open/closed straight wings from pitching/plunging motions. All motions has one degree amplitude and a reduced frequency of 0.1. In plunging motions $q = 0$.



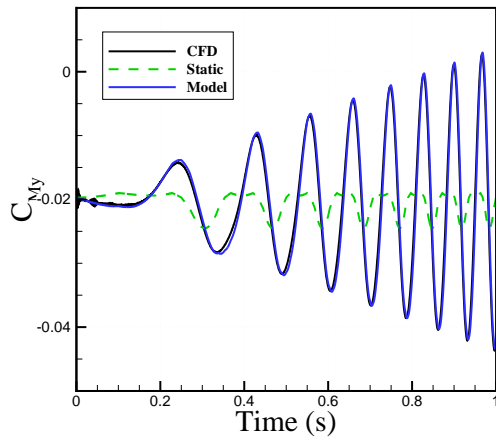
(a) A chirp motion



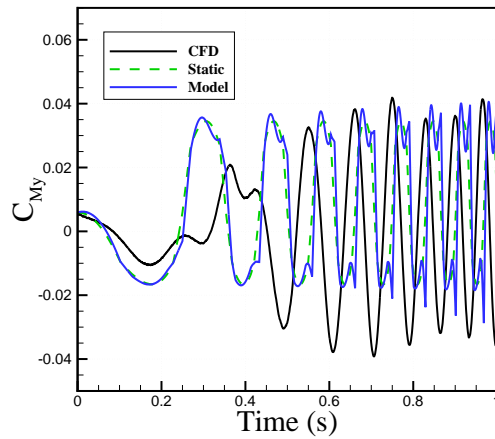
(b) SR, lift coefficient



(c) OpenS, lift coefficient



(d) SR, pitch moment coefficient



(e) OpenS, pitch moment coefficient

Figure 13. Aerodynamic modeling of the open/closed straight wings for a chirp motions.